



# Time Variability of FUV Emission from Cool Stars on Multi-year Timescales

Leo Kamgar<sup>1</sup> , Kevin France<sup>1</sup> , and Allison Youngblood<sup>2</sup>

<sup>1</sup> Laboratory for Atmospheric and Space Physics, University of Colorado Boulder, Boulder, CO 80303, USA; [leokamgar@gmail.com](mailto:leokamgar@gmail.com)

<sup>2</sup> Exoplanets and Stellar Astrophysics Lab, NASA Goddard Space Flight Center, Greenbelt, MD 20771, USA

Received 2023 August 18; accepted 2023 December 1; published 2024 February 20

## Abstract

The physical and chemical properties of planetary atmospheres are affected by temporal evolution of ultraviolet (UV) radiation inputs from their host stars at all time scales. While studies of X-ray/UV flare properties and long-term stellar evolution of exoplanet host stars have provided new constraints regarding stellar inputs to exoplanetary systems, the UV temporal variability of cool stars on the timescale of stellar cycles remains largely unexplored. To address this gap in our understanding of the UV temporal variability of cool stars, we analyze far-ultraviolet (FUV) emission lines of ions that trace the chromosphere and transition region of nearby stars (C II, Si III, Si IV, and N V; formation temperatures  $\sim 20\text{--}150$  kK) using data from the Hubble Space Telescope (HST) and International Ultraviolet Explorer (IUE) archives spanning temporal baselines of months to years. We select 33 unique stars of spectral types F-M with observing campaigns spanning over a year, and create ionic light curves to evaluate the characteristic variability of cool stars on such timescales. Screening for large flare events, we observe that the relative variability of FUV light curves decreases with increasing stellar effective temperature, from 30% to 70% variability for M-type stars to  $<30\%$  variability for F and G-type stars. We also observe a weak trend in the temporal variability with the Ca II  $R'_{HK}$  stellar activity indicator, suggesting that stars with lower Ca II activity exhibit a smaller range of FUV flux variability. Screening for data sets with optimal temporal spread, and a sufficient number of individual observations, we select 5 data sets for further periodicity analysis (HST  $\alpha$  Centauri A, HST  $\alpha$  Centauri B, IUE  $\alpha$  Centauri B, IUE  $\epsilon$  Eri, IUE  $\xi$  Boo). Various periodic structures within the FUV flux were detected, with most significant being a 79 days frequency present within the IUE observations of  $\xi$  Boo, with a significance of  $6\sigma$ , and a periodic signal in the FUV observations of  $\alpha$  Centauri B, for both HST and IUE measurements, at  $\approx 210$  days frequency with significance of  $3\sigma$  and  $3.7\sigma$ , respectively. Our results suggest that extreme ultraviolet flux from cool stars varies by less than a factor of two on decade timescales, significantly smaller than variations on flare or stellar evolutionary timescales.

*Unified Astronomy Thesaurus concepts:* [Ultraviolet telescopes \(1743\)](#); [Stellar activity \(1580\)](#); [Stellar chromospheres \(230\)](#)

## 1. Introduction

As a result of the ever-expanding number and diversity of exoplanet detections and the introduction of powerful new observatories such as the James Webb Space Telescope, astronomy has entered the era of exoplanet atmospheric characterization. The study of exoplanet atmospheric evolution is needed to understand how their properties evolve over the lifetimes of these planets. Therefore our goal has pivoted toward analyzing and understanding exoplanetary atmospheric composition and evolution. This can then inform the search for planets that may potentially support habitable atmospheric conditions.

Of the factors that drive atmospheric composition and evolution, one of the most critical is the interaction between exoplanetary atmospheres and their host star's light. Starlight is the primary energy source that drives photochemistry, heating, and cooling within atmospheres (Tsai et al. 2023). The

radiative transfer properties of these exoplanetary atmospheres are determined by the absorption and scattering of light by atmospheric gases. This process then influences the temperature and pressure profiles of these planets. Furthermore, the interactions between starlight and exoplanetary atmospheres drive atmospheric escape processes, which can be a dominant factor in the evolution of these planets (Lammer et al. 2003; Airapetian et al. 2020).

Ultraviolet (UV) radiation plays a central role in the photochemical reactions on both gaseous and rocky exoplanets. UV photons ionize and dissociate molecular species in the upper atmosphere, which in turn leads to the formation of radicals and ions. These molecular species can then participate in numerous chemical reactions (Miguel & Kaltenegger 2014; Tsai et al. 2023).

For rocky planets, UV radiation is a driving factor in the formation of ozone, a molecule necessary for blocking harmful

UV radiation from reaching the surface of a planet. Ozone, is formed by a series of photochemical reactions that begin with the dissociation of carbon dioxide and molecular oxygen by UV. These resulting oxygen atoms will react with molecular oxygen to form ozone (Harman et al. 2015).

In addition to UV's contribution on rocky planets, it is a significant source of formation of haze particles in the upper atmosphere of Jovian and Neptunian planets. These haze particles are formed by photochemical processes involving simple organic molecules, such as methane and nitrogen, by high-energy photons. The precise mechanisms involved with haze formation are not completely understood. However, it is thought to involve complex photochemical pathways that produce a range of organic molecules, some of which can condense into small particles that scatter light (see, e.g., Teal et al. 2022 and references therein).

Exposure to high-energy stellar radiation also heats a planet's atmosphere. This increase in temperature directly increases the atmospheric escape rate. High-energy photons ionize and dissociate atmospheric species, imparting kinetic energy (heat) to the gas in the process. When an atmosphere becomes heated, gaseous atoms within the atmosphere begin to move faster. These faster speeds allow for more energetic atoms to escape the atmosphere completely, leading to greater atmospheric escape rates. This process can ultimately lead to a planet losing its atmosphere entirely, likely rendering it uninhabitable (Tian et al. 2008; Jakosky et al. 2018).

Generation of UV radiation in the stellar atmosphere is directly linked to the energy input into the atmosphere by magnetic heating processes. This heating, in turn, is followed by higher electron collision rates, leading to a highly ionized plasma.  $\text{Si}^{2+}$ ,  $\text{N}^{4+}$ ,  $\text{C}^+$ , and  $\text{Si}^{3+}$  ions are formed within the chromosphere and transition region of a star, where they emit the spectroscopic tracers Si III, N V, C II, and Si IV (corresponding to each ion, respectively), which in turn serve as probes of the stellar UV radiation.

FGKM stars, which include F, G, K, and M spectral types, make up  $\sim 90\%$  of stars, and are commonly known as “cool stars.” They are of particular interest to astronomers for their similarities with our own Sun in terms of size, mass, and temperature. The mass range of FGKM stars is approximately  $\sim 2\text{--}0.1M_{\text{Sun}}$ , with F stars being the most massive of this group ( $\sim 1\text{--}2M_{\text{Sun}}$ ) and M stars being the least massive ( $\sim 0.1\text{--}0.6M_{\text{Sun}}$ ). Because FGKM stars are relatively smaller and cooler than larger, hotter stars, they are favorable for the transit method of exoplanet detection (where the signal is proportional to the ratio of the planetary to stellar surface area).

The increased emphasis in exoplanet atmospheric characterization has highlighted a gap in our knowledge of cool stars and their temporal variability. Although numerous studies on the UV variability associated with flares and long-term evolution have been analyzed (see France et al. 2018; Loyd et al. 2018a, 2018b; Pineda et al. 2021; Jackman et al. 2023 and references therein),

there are few comprehensive studies on the longer-term UV temporal variability of cool stars (e.g., Ayres 1991; Loyd et al. 2023). As a result, less is known about the UV variability of planet-hosting stars on timescales of stellar rotation or planetary orbits, e.g., timescales of months to years.

In efforts to address this gap, this work aims to provide information on the longer-term temporal variability of cool stars, which can provide inputs to planetary atmosphere evolution models and aid in the prioritization of stars for the observation of all types of exoplanets. With the use of direct imaging techniques planned for the Habitable Worlds Observatory, NASA requires information that better determines which stars are the most promising targets to maximize the chances of detecting and characterizing habitable exoplanets. This study will provide inputs to NASA's target selection and habitable planet detection strategies for future missions.

This paper presents an investigation of the temporal UV variability of cool stars on timescales of months to years with an archival study of UV spectroscopic observations made over the long missions of the Hubble Space Telescope (HST) and the International Ultraviolet Explorer (IUE). This study analyzes the emission lines Si III, N V, C II, and Si IV, spectral features. By analyzing how these spectral emission features evolve in time, this study characterizes the UV variability of these stars and explores the correlation with the degree of UV variability with the mass and magnetic activity levels of the stellar sample.

## 2. UV Spectroscopic Observations and Data Reduction

We first conducted a comprehensive search of the Mikulski Archive for Space Telescopes (MAST) to identify multi-epoch far-ultraviolet (FUV) spectroscopic observations of cool stars of spectral types F-M. There was strict criteria imposed on the search, being that the mission must contain long-term (Periods spanning greater than 1 yr) data observation of a star with simultaneous coverage over a range of formation temperatures (C II, Si III, Si IV, N V emission lines, corresponding to a range in formation temperatures  $T_{\text{form}} \sim 20\text{--}150 \text{ kK}$ ). The missions that met the requirements were the HST-Space Telescope Imaging Spectrograph (STIS) and -Cosmic Origins Spectrograph (COS) instruments, as well as the IUE. Many other FUV spectroscopic instruments, such as the Hopkins Ultraviolet Telescope, and earlier generation UV spectrographs on HST lacked either the necessary long-term multi-epoch data sets, or spectral coverage, which hindered a uniform data set for emission line monitoring. Following France et al. (2018), we focus on the ionic emission lines of Si III, N V, C II, and Si IV, which are visible at wavelengths, 1206 Å, 1238, 1243 Å, 1334, 1335 Å, and 1394, 1403 Å, and corresponding  $\log_{10}(T_{\text{form}})$ 's of 4.7, 5.2, 4.5, and 4.8, respectively ( $T_{\text{form}}$  is the formation temperature of the ion that generates the emission line). For the

stars observed by HST, all four emission lines were clearly distinguished from the background in the data. For IUE, many of the N V and Si III lines were overwhelmed by scatter from the nearby, bright geocoronal Ly $\alpha$  emission line (France et al. 2016), and we therefore only consider C II and Si IV emission measurements from the IUE data.

We restricted our analysis to objects with FUV spectroscopic data sets covering a temporal baseline of at least one year (the average returned data set spans 3793 days), with a minimum of five individual visits to the target in total. Following this, an initial visual inspection was then conducted on a subset of each target's spectroscopic data to ensure the data quality would be high enough for reliable emission line measurements. With these filters and inspections in place, numerous cool star monitoring programs from IUE (Ayres 1991), and exoplanet host star monitoring or transit programs with HST (MacGregor et al. 2021; Loyd et al. 2023), were identified. The final list of potential targets then underwent an additional screening for interacting binary stars (e.g., RS CVn systems) before downloading the full multi-epoch data sets from MAST. Ultimately, this process had yielded a final sample of 9 stars from HST and 29 stars from IUE, with some stars overlapping both data sets. Other binary stars not indicated as interactive or RS CVn systems in the Simbad database are left in the sample as these stars are expected to undergo variability in the same mode as single stars. The stellar sample, with associated stellar parameters presented in Table 1, is presented in Table 2, with temporal baselines ranging from approximately 1 to 20 yr and 5–200 visits per star.

Spectral analysis was conducted on a per-exposure basis, in order to extract the relevant emission line fluxes of the four ionic transitions tracing the chromosphere and transition region. For the instruments employing first-order spectrometers (HST-COS and IUE), the flux and wavelength-calibrated data were able to be directly analyzed. However, for HST-STIS echelle data, the multiple orders of data were combined into a single one-dimensional flux and wavelength-calibrated spectrum prior to analyzing the emission lines. In order to measure the emission line fluxes, numerical integration was performed on the wavelength region containing the line of interest (visible in the red regions in Figures 1 and 2) and stored as  $F_{\text{ion}}$ . The uncertainty within the measurement is stored as  $\text{Err}_{\text{ion}}$ , before subtracting a nearby continuum/background region of the same spectral width (visible in the orange regions in Figures 1 and 2) and stored as  $B_{\text{ion}}$ . In effort to minimize randomized noise and poor data measurements, further data refinement occurred. Because our sample contained significantly more photospheric continuum emission as the target spectral type moved from M to F, but this background was stellar signal and not instrumental background noise, we reduced the detection threshold level above the continuum accordingly. Therefore, setting a detection threshold for including an individual measurement of  $k$ , a filter for data points is as provided:  $F_{\text{ion},k} - \text{Err}_{\text{ion},k} > 1.3\text{--}2.0 \times B_{\text{ion},k}$ , depending on the spectral type of the target star. Subsequently,

**Table 1**  
Star Parameters

Star	$B - V$	$T_{\text{eff}}$	$P_{\text{rot}}$	$\log(R'_{\text{HK}})$
$\alpha$ CMi	0.42	6474	23	-4.11
$\beta$ Cas	0.34	6959	1.1	-4.27
BH CVn	0.4	6653	...	-3.84
$\epsilon$ Aur	0.54	7395	...	...
$\epsilon$ CrA	0.36	6647	...	...
h UMa	0.33	7096	0.85	-3.99
$\alpha$ Centauri A	0.71	5788	...	-5.15
HD 209458	0.58	6118	14.4	-4.88
E Vir	...	5999	3.3	-4.30
AR Lac	0.72	5342	...	...
EK Dra	0.639	5845	2.606	-4.02
$\xi$ Boo	0.777	5511	6.43	-4.30
$\alpha$ Centauri B	0.88	...	36.2	-4.97
HD 189733	0.93	5044	13.4	-4.51
AB Dor	0.857	5273	0.5	-3.88
CC Eri	1.336	3831	...	-3.78
$\epsilon$ Eri	0.88	...	11.7	-4.51
36 Oph B	0.85	5199	...	-4.74
70 Oph	0.86	5419	19.7	-4.12
HD 17925	0.86	5115	6.6	-4.30
LQ Hya	0.87	...	1.6	-3.97
UX Ari	0.91	5041	6.4	...
HD 283750	...	4405	1.8	...
AU Mic	1.423	3518	4.85	-3.88
Ross 905	1.447	3353	48	-5.09
Proxima Centauri	1.82	2810	83	-4.30
BD+20 2465	1.3	2991	...	-4.00
BD+19 5116	1.584	3630	1.06	...
EV Lac	1.59	3167	...	-3.75
HD 152751	1.57	3441	...	-4.20
V1005 Ori	1.373	3661	4.4	...
YY Gem	1.29	3885	...	...
YZ CMi	1.606	3088	2.77	-3.47

**Note.** Star parameter data for each unique star within study.  $T_{\text{eff}}$  (Effective Temperature) is measured in (K) and  $P_{\text{rot}}$  (Rotational Period) in (days). Sources: (1) SIMBAD Astronomical Database (<https://simbad.u-strasbg.fr/simbad/sim-fbasic>), (2) Boro Saikia et al. (2018).

arrays of line fluxes measured were analyzed for data quality issues, such as guide star acquisition failures that result in the stellar flux being comparable to the background level (excluding points with  $F_{\text{ion},k} < 0.2 \langle F_{\text{ion}} \rangle$ ). Finally, these time-resolved emission line fluxes constitute the spectroscopic lightcurves (Figures 3(a)–(d)) that were then analyzed for further understanding of the long-term variability of the FUV output of nearby cool stars, as described in Section 3.

### 3. FUV Lightcurves and Analysis

#### 3.1. Relative Variability/Maximum Linear Regression Analysis

In the context of quantifying the impact on exoplanetary atmospheres, we are interested in the typical degree of

**Table 2**  
Star Data Collection

Star	Instr.	<i>N</i>	Start	End	$\Delta$
$\beta$ Cas	IUE	50	43743.2	48822.7	5079.5
BH CVn	IUE	6	44024.7	49166.8	5142.1
$\epsilon$ Aur	IUE	84	43731.7	46156.0	2424.3
h UMa	IUE	3	47963.9	49389.9	1426.0
$\alpha$ CMi	HST	5	55656.109	55864.76	208.651
$\epsilon$ CrA	IUE	16	44157.4	45056.7	899.3
AR Lac	IUE	223	44011.4	49631.5	5620.1
EK Dra	IUE	18	45152.2	49893.3	4741.1
$\alpha$ Centauri A	IUE	188	43737.2	49935.6	6198.4
E Vir	IUE	20	45011.6	49890.8	4879.2
HD 209458	HST	21	55093.424	57520.977	2427.553
$\xi$ Boo	IUE	62	43644.4	49132.9	5488.5
$\alpha$ Centauri A	HST	15	55220.219	58011.661	2791.442
$\epsilon$ Eri	IUE	73	43743.6	48480.7	4737.1
$\alpha$ Centauri B	IUE	77	43737.5	49931.6	6194.1
LQ Hya	IUE	26	45283.2	49345.1	4061.9
36 Oph B	IUE	3	44506.4	48136.5	3630.1
CC Eri	IUE	19	47795.8	48251.7	455.9
UX Ari	IUE	66	43735.6	50104.9	6369.3
$\alpha$ Centauri B	HST	9	55378.037	56862.925	1484.888
HD 189733	HST	8	55090.772	59093.266	4002.494
HD 17925	IUE	13	44892.4	49694.9	4802.5
70 Oph	IUE	15	44436.8	48148.0	3711.2
AB Dor	IUE	30	45082.0	48255.8	3173.8
HD 283750	IUE	10	44611.0	48660.9	4049.9
HD 152751	IUE	13	44466.0	48314.6	3848.6
HD 197481	HST	4	51062.512	51062.704	0.192
Ross 905	HST	15	56101.308	58177.314	2076.006
Proxima Centauri	HST	54	51672.04	58665.058	6993.018
BD+20 2465	HST	6	51613.145	52427.233	814.088
EV Lac	IUE	20	44849.6	49241.7	4392.1
HD197481	IUE	82	44122.8	48874.6	4751.8
BD+19 5116	IUE	22	43858.0	48861.9	5003.9
Proxima Centauri	IUE	14	43921.7	49927.7	6006.0
YZ CMi	IUE	40	43922.1	49708.2	5786.1
V1005 Ori	IUE	10	44525.7	48677.9	4152.2
YY Gem	IUE	63	45303.4	48349.3	3045.9
BD+20 2465	IUE	57	45138.7	48385.2	3246.5

**Note.** Star data collection statistics. Instr. indicates the instrument used for measurement. *N* is number of total measurements. Start and End are the Modified Julian Date days of the first and last measurement, respectively.  $\Delta$  in (days), is the length of observation.

variability exhibited by cool stars (as a function of their mass and activity levels) as well as the extrema of these behaviors which may drive changes in the local conditions in planetary atmospheres (e.g., France et al. 2020; Chen et al. 2021). The calculations for the relative variability and maximum variability were computed by performing standard statistical techniques on the various samples of data. In practice, these calculations for the HST and IUE data were processed via the numpy (Harris et al. 2020) software package. Starting with a

flux-calibrated light curve for each ion:

$$\{[t_1, f_1 \pm E[f_1]], \dots, [t_n, f_n \pm E[f_n]]\}_{\text{ion}}$$

where  $f_i$  denotes some measured flux output (of which there are  $n$  measurements), with associated measurement error,  $E[f_i]$ , corresponding to the time of measurement,  $t_i$ . We start with the sample mean,  $\mu$ , standard deviation,  $\sigma$ , and maximum,  $\alpha$ , for each ion:

$$\mu = \frac{\sum_{i=1}^n f_i}{n} \quad (1)$$

$$\sigma = \sqrt{\frac{\sum_{i=1}^n (f_i - \mu)^2}{n}} \quad (2)$$

$$\alpha = \text{Max}\{f_1, \dots, f_n\}. \quad (3)$$

Given these statistical variables, we define the relative variability,  $\sigma_{\text{rel}}$ , and relative maximum,  $\alpha_{\text{rel}}$ , as:

$$\sigma_{\text{rel}} \equiv \frac{\sigma}{\mu} \quad (4)$$

$$\alpha_{\text{rel}} \equiv \frac{\alpha}{\mu}. \quad (5)$$

In order to get the associated errors with each of these calculated variables, we use the division and multivariate error propagation formulas. These formulae yield error formulas for the following variables:

$$E[\sigma_{\text{rel}}] \approx \sigma_{\text{rel}} \sqrt{\frac{\sum_{i=1}^n (f_i - \mu)^2 E[f_i]^2}{n^2 \sigma^4} + \frac{\sigma_{\text{rel}}^2}{n}} \quad (6)$$

$$E[\alpha_{\text{rel}}] = \alpha_{\text{rel}} \sqrt{\left(\frac{E[f_j]}{\alpha}\right)^2 + \frac{\sigma_{\text{rel}}^2}{n}}. \quad (7)$$

Provided with the relative variability, relative maximum, their associated errors, and stellar parameters, we compute the linear regression fits between the UV observables and the stellar characteristics (Table 1) using numpy polyfit.

Using the relative variability, relative maximum, their associated errors, presented in Table 3, and the solutions for the best-fit line parameters, we consider the relationships between the relative variability and relative maximum with various star parameters:  $B - V$  magnitude (tracer of the effective temperature of a star), direct effective temperature measurements from the literature based on a combination of photometric and spectroscopic observations, rotational period, and  $\log(R'_{\text{HK}})$  (chromospheric contribution to the stellar spectrum near the Ca II H and K lines). The best-fit parameters for relative variability versus effective temperature are presented in Table 4.

Upon careful examination of the trends within the best-fit lines, it is apparent that the linear models produced with fits weighted by  $\frac{1}{\text{Error}^2}$  are overweighted by the fact that the nearest,

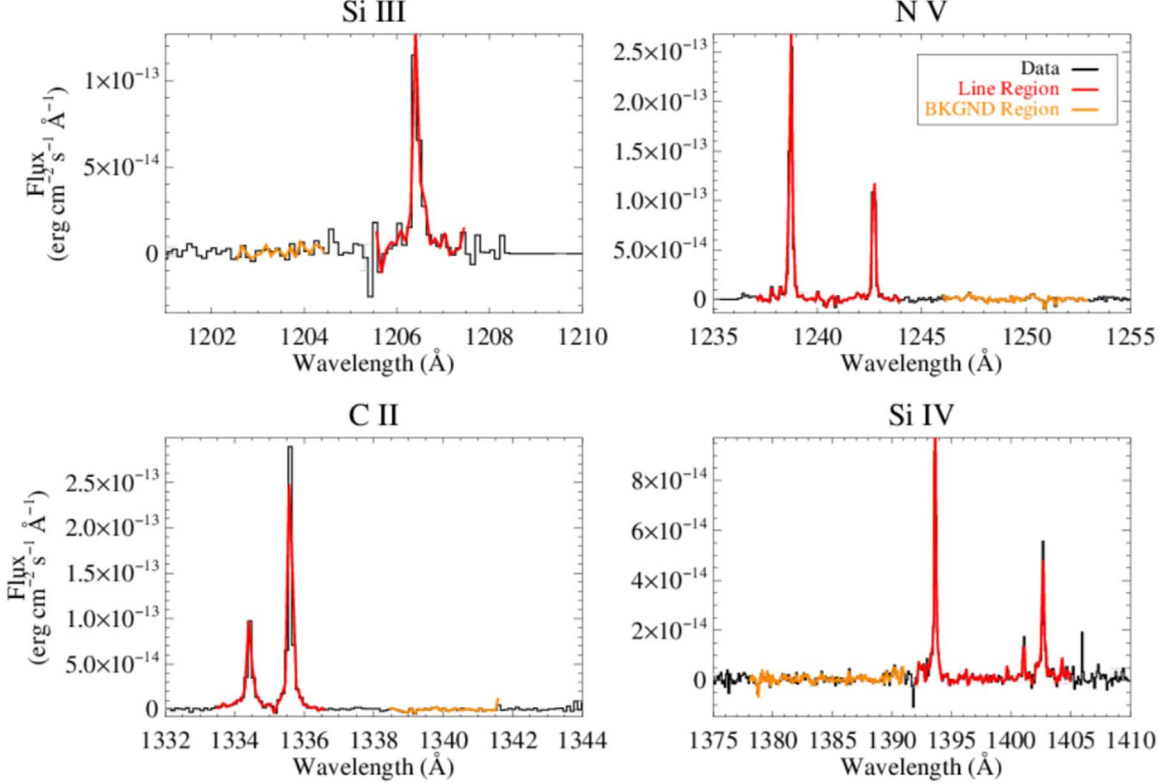


**Figure 1.** Example HST-STIS spectra of Proxima Cen (M5.5 V) showing the emission line measurement regions around Si III, N V, C II, and Si IV. The black histogram is the STIS E140M data. The final emission fluxes are the numerically integrated on-line region (shown in red) with the nearby instrumental/continuum background subtracted (the background region is shown in orange).

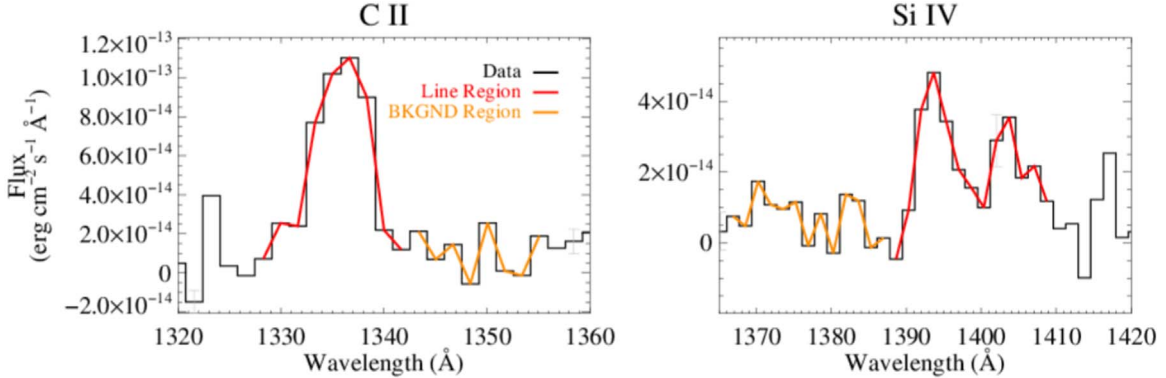
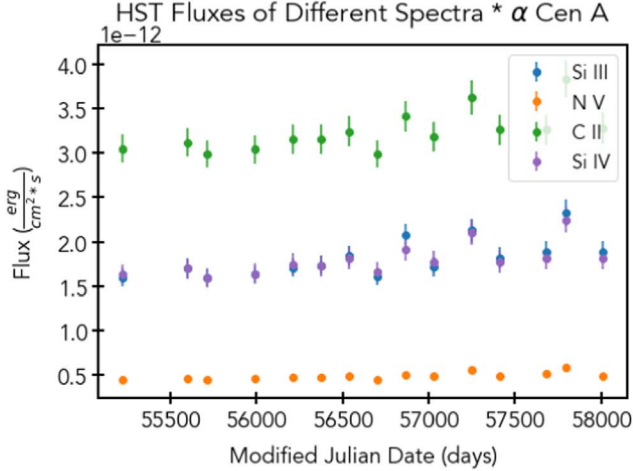


**Figure 2.** Example IUE spectrum of  $\epsilon$  Eri (K2 V) showing the emission line measurement regions around C II and Si IV. The black histogram is the IUE data. The final emission fluxes are the numerically integrated on-line region (shown in red) with the nearby instrumental/continuum background subtracted (the background region is shown in orange). We do not measure Si III and N V in the IUE data owing to a large contribution from scattered geocoronal and stellar Ly $\alpha$ .

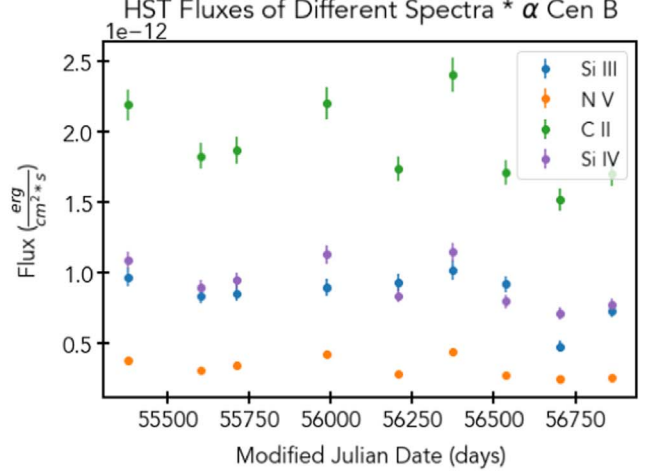
brightest stars (with the smallest photometric uncertainty in their lightcurves) are low activity stars with very low relative variability. The “high-signal-to-noise ratio” points prevent the regression fit from thoroughly sampling the higher relative uncertainty points at lower effect temperatures, essentially preventing the regression fits from considering the contribution

from fainter K and M stars. For this reason, we consider the unweighted linear regression fits in this analysis.

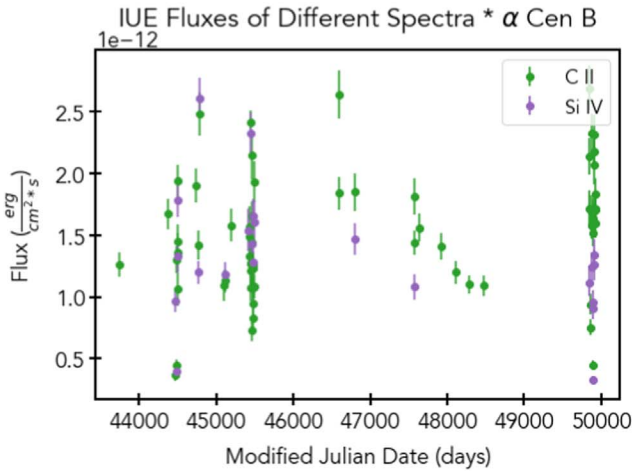
Close binary star systems were included in the relative maximum plots to indicate the maximum deviations from the quiescent flux that could be expected individual exposures, but these sources were excluded from the relative variability plots



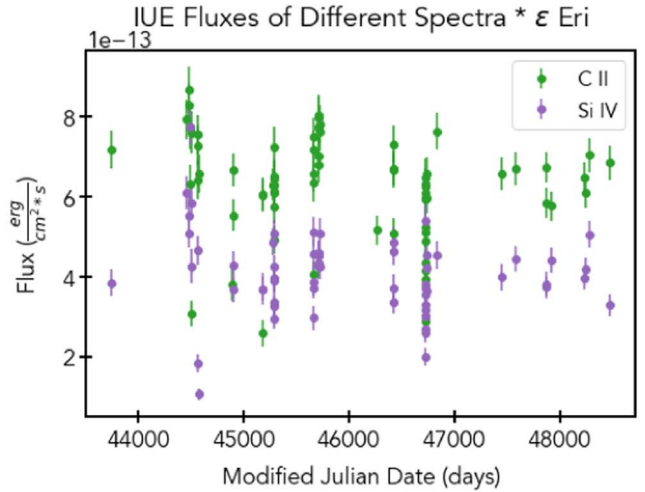
(a) *HST* Flux measurements of  $\alpha$  Cen A, for Si III, N V, C II, and Si IV ion emission bands.



(b) *HST* Flux measurements of  $\alpha$  Cen B, for Si III, N V, C II, and Si IV ion emission bands.



(c) *IUE* Flux measurements of  $\alpha$  Cen B, for C II and Si IV ion emission bands.



(d) *IUE* Flux measurements of  $\epsilon$  Eri, for C II and Si IV ion emission bands.

**Figure 3.** *HST* and *IUE* time-series flux measurements of various stars.

and the related linear fits. Close binary systems display enhanced UV activity owing to the interaction of their magnetospheres, which are not representative of single-star systems that are the primary focus of this work.

Examining relative variability subplots of Figure 4, we observe significant correlations between relative variability and various stellar parameters. Specifically, Figure 4(a) indicates a positive correlation ( $\sim 2.5\sigma$ , defined as the number of standard deviations by which the slope coefficient exceeded zero) between relative variability and  $B - V$  color, while Figure 4(c) shows a negative relationship ( $\sim 3\sigma$ ) between relative variability and effective temperature (confirming the trend observed in Figure 4(a)). Additionally, Figure 4(e) reveals a positive

relationship ( $\sim 2.2\sigma$ ) between relative variability and rotational period. Upon further analysis of this relationship, however, it is revealed that a singular outlier point was driving this relationship. Without this point (dashed line in Figure 4(e)), we see a weak negative correlation ( $\sim 0.7\sigma$ ) between relative variability and rotational period. Figure 4(g) also demonstrates a weak correlation ( $\sim 1.4\sigma$ ) between relative variability and  $\log(R'_{HK})$ .

There are certain outlier stars in the relative maximum panels of Figure 4 that demonstrate notably large relative maxima, reaching as high as  $\sim 3.5\text{--}5.5 \times$  the mean. These outliers correspond to stars with strong stellar flare activity, particularly low-mass single-star systems (M type dwarfs) and interacting binary systems. The interaction between companion stars in

**Table 3**  
C II Relative Variabilities and Maxima

Star	Telescope	$\sigma_{\text{rel}}$	$\alpha_{\text{rel}}$
$\beta$ Cas	IUE	$0.2517 \pm 0.0294$	$1.6865 \pm 0.2291$
BH CVn	IUE	$0.2138 \pm 0.0445$	$1.3017 \pm 0.1643$
$\epsilon$ Aur	IUE	$0.8495 \pm 0.168$	$4.884 \pm 0.9719$
$\alpha$ CMi	HST	$0.0565 \pm 0.027$	$1.0954 \pm 0.0695$
$\epsilon$ CrA	IUE	$0.1804 \pm 0.027$	$1.2872 \pm 0.1129$
AR Lac	IUE	$0.2957 \pm 0.0103$	$3.3849 \pm 0.2082$
EK Dra	IUE	$0.1982 \pm 0.0206$	$1.3859 \pm 0.1116$
$\alpha$ Cen A	HST	$0.0694 \pm 0.0149$	$1.1826 \pm 0.0659$
$\alpha$ Cen A	IUE	$0.5057 \pm 0.0435$	$3.223 \pm 0.3609$
E Vir	IUE	$0.2403 \pm 0.0235$	$1.3888 \pm 0.1095$
HD 209458	HST	$0.1057 \pm 0.0206$	$1.181 \pm 0.138$
$\xi$ Boo	IUE	$0.1376 \pm 0.0101$	$1.4726 \pm 0.1032$
$\epsilon$ Eri	IUE	$0.2034 \pm 0.0092$	$1.3787 \pm 0.0965$
$\alpha$ Cen B	HST	$0.1437 \pm 0.0198$	$1.2587 \pm 0.0883$
$\alpha$ Cen B	IUE	$0.3348 \pm 0.0174$	$1.8005 \pm 0.1418$
LQ Hya	IUE	$0.8294 \pm 0.1777$	$4.0839 \pm 0.8671$
36 Oph B	IUE	$0.0995 \pm 0.0417$	$1.104 \pm 0.0967$
CC Eri	IUE	$0.199 \pm 0.0203$	$1.4455 \pm 0.1148$
UX Ari	IUE	$0.3581 \pm 0.0209$	$2.0857 \pm 0.1564$
HD 189733	HST	$0.1006 \pm 0.0185$	$1.1185 \pm 0.0724$
HD 17925	IUE	$0.1539 \pm 0.0195$	$1.3128 \pm 0.0924$
70 Oph	IUE	$0.1854 \pm 0.0215$	$1.2861 \pm 0.1059$
AB Dor	IUE	$0.1496 \pm 0.0124$	$1.2755 \pm 0.0808$
HD 283750	IUE	$0.1706 \pm 0.0263$	$1.416 \pm 0.1149$
HD 152751	IUE	$0.1809 \pm 0.0292$	$1.3034 \pm 0.121$
Ross 905	HST	$0.2039 \pm 0.0325$	$1.4512 \pm 0.1339$
Proxima Centauri	HST	$0.5755 \pm 0.058$	$3.144 \pm 0.3434$
Proxima Centauri	IUE	$0.7654 \pm 0.2965$	$2.0496 \pm 0.7933$
BD+20 2465	HST	$0.0657 \pm 0.0229$	$1.1267 \pm 0.0665$
BD+20 2465	IUE	$0.4111 \pm 0.048$	$2.7123 \pm 0.3036$
EV Lac	IUE	$0.3974 \pm 0.0667$	$1.5402 \pm 0.2492$
BD+19 5116	IUE	$0.2642 \pm 0.0318$	$1.4995 \pm 0.1461$
YZ CMi	IUE	$0.4501 \pm 0.077$	$1.8149 \pm 0.314$
V1005 Ori	IUE	$0.5231 \pm 0.1739$	$1.6354 \pm 0.5236$
YY Gem	IUE	$0.2585 \pm 0.027$	$1.5291 \pm 0.1846$
HD 197481	HST	$0.0536 \pm 0.0294$	$1.0913 \pm 0.0674$
HD 197481	IUE	$0.426 \pm 0.0302$	$1.8887 \pm 0.1784$

**Note.** Relative variability ( $\sigma_{\text{rel}}$ ) and relative maximum ( $\alpha_{\text{rel}}$ ) calculated for corresponding telescope and C II ion emission band. These are subsequently plotted against various star parameters within Figure 4.

**Table 4**  
Linear Regression Parameters for Relative Variability vs. Effective Temperature

Ions	$\beta_0$ (1)	$\beta_1$ (2)
Si III	$0.28 \pm 0.13$	$(-3.07 \pm 2.60) * 10^{-5}$
N	$0.33 \pm 0.15$	$(-4.52 \pm 3.10) * 10^{-5}$
C II	$0.54 \pm 0.10$	$(-6.59 \pm 2.19) * 10^{-5}$
Si IV	$0.65 \pm 0.11$	$(-7.17 \pm 2.37) * 10^{-5}$

**Note.**  $\beta_0$  refers to the intercept parameter, and  $\beta_1$  refers to the slope parameter for the given weighted linear regression. These are visible within Figures 4, 7, 8, 9 subplots C.

binary systems, such as the RS CVn systems mentioned in Section 2, can lead to enhanced magnetic activity and flare magnitudes, resulting in greater relative maximums (Osten & Brown 1999). Furthermore, these trends persist additional ion emission bands, in Figures 7–9.

### 3.2. FUV Periodicity: Lomb–Scargle Analysis

Further analysis of the FUV light curves were provided in efforts of exploring periodic variability that may be indicative of stellar activity cycles within these stars. Beginning with the FUV light curves, we utilized the Fourier transform for a complete frequency deconstruction of the underlying flux signal. Fourier transforms work on the principle that any periodic function (in this case, the flux signal) can be broken down into an infinite sum of sine and cosine waves. The analysis of the makeup of sine and cosine waves of varying frequencies then provide understanding about the stellar activity itself. As such, the Fourier transform becomes the natural solution when considering the statistical analysis of frequencies present within each lightcurve.

There are certain drawbacks, however, when utilizing Fourier transforms. They follow the assumption that the underlying signal is perfectly periodic, which is not always entirely true. Additionally, given the relatively small amount of measurements within the flux light curves, as well as clustering within time, the Fourier transform may introduce significant noise into frequency deconstruction.

In remediation of these constraints, we utilized wavelet transforms for signal denoising. This mathematical method decomposes signals into wavelets, which are localized in both frequency and time domains. This collection of wavelets used for transformation are an orthonormal set of basis functions defined by some given wavelet function, as well as its associated scaling function.

Wavelet transforms can capture both high and low frequency components of a signal, isolate their influences on the entirety of the signal, and their associated temporal evolution. As such, wavelets become a natural solution toward dampening the effects of signal noise present within the output of the Fourier transform frequency decompositions. The specific technique utilized, soft thresholding, removes or shrinks coefficients that correspond to noise present within the input (represented by smaller wavelet coefficients below a threshold), leaving only those representing the signal largely unaffected.

Additionally, many data sets available within our sampling of stars provide for poor data for periodicity analysis. This is due to the particular data distributions necessary for the Fourier transform, being a wide distribution of data points across time, in non-periodic measurements. Greater time spread provides better frequency resolution, and non-periodic measurements negate the false periodic signals that would become present

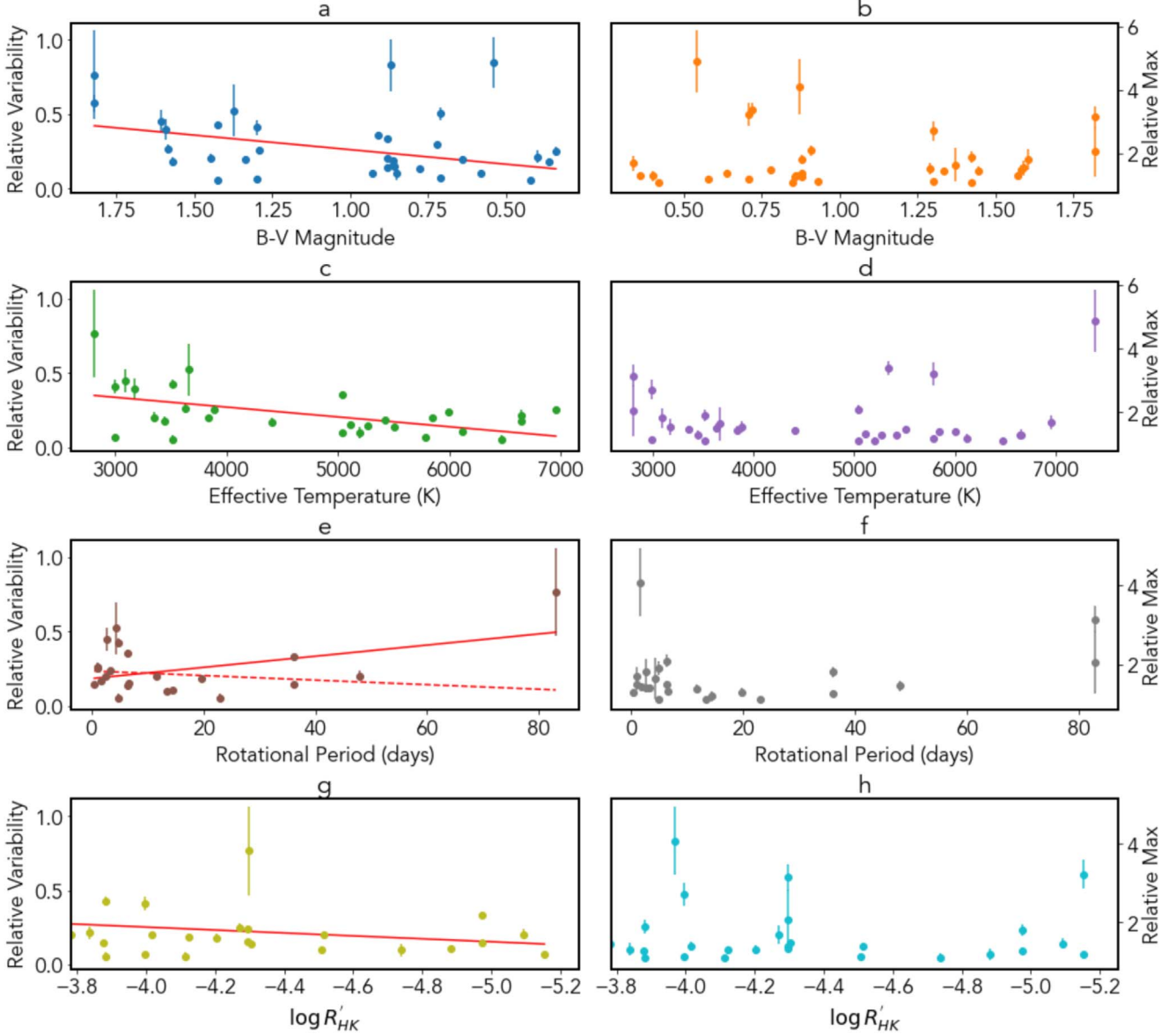


**Figure 4.** Left: correlations of C II ion emission variability vs. various stellar parameters with unweighted linear regression depicted with the red lines. Figure (E) contains additional unweighted linear regression (dashed red line) that does not include the outlier point, Proxima Centauri, in regression analysis. Right: relative maximum (maximum divided by the mean) of C II ion emission vs. various stellar parameters.

within the transform. As a result, our study focuses on 5 ideal data sets for periodicity analysis, HST  $\alpha$  Centauri A, HST  $\alpha$  Centauri B, IUE  $\alpha$  Centauri B, IUE  $\epsilon$  Eri, and IUE  $\xi$  Boo, due to their wide spread in the time-domain, non-periodic measurements, and great number of measurements.

To perform discrete Fourier transform computations on our data sets, we utilized the Lomb–Scargle Periodogram sub-package of the astropy package (Astropy Collaboration et al. 2022). Additionally, we utilized the PyWavelets package (Lee et al. 2019) for wavelet denoising. From this, we are able to

transform the flux as a function of time, Figure 3(a), into frequencies and their associated power spectrum, Figure 5. Figure 5 shows the deconstruction of each individual ion flux time series into its frequency domain (left-most column), as well as increasingly greater levels of soft thresholding (columns to the right). Each successive column's threshold is calculated via the keep coefficient, which dictates the percentage of wavelet coefficients to be kept after the soft thresholding (e.g., 1 indicates no denoising, 0.5 indicates 50% of wavelet coefficients are kept).

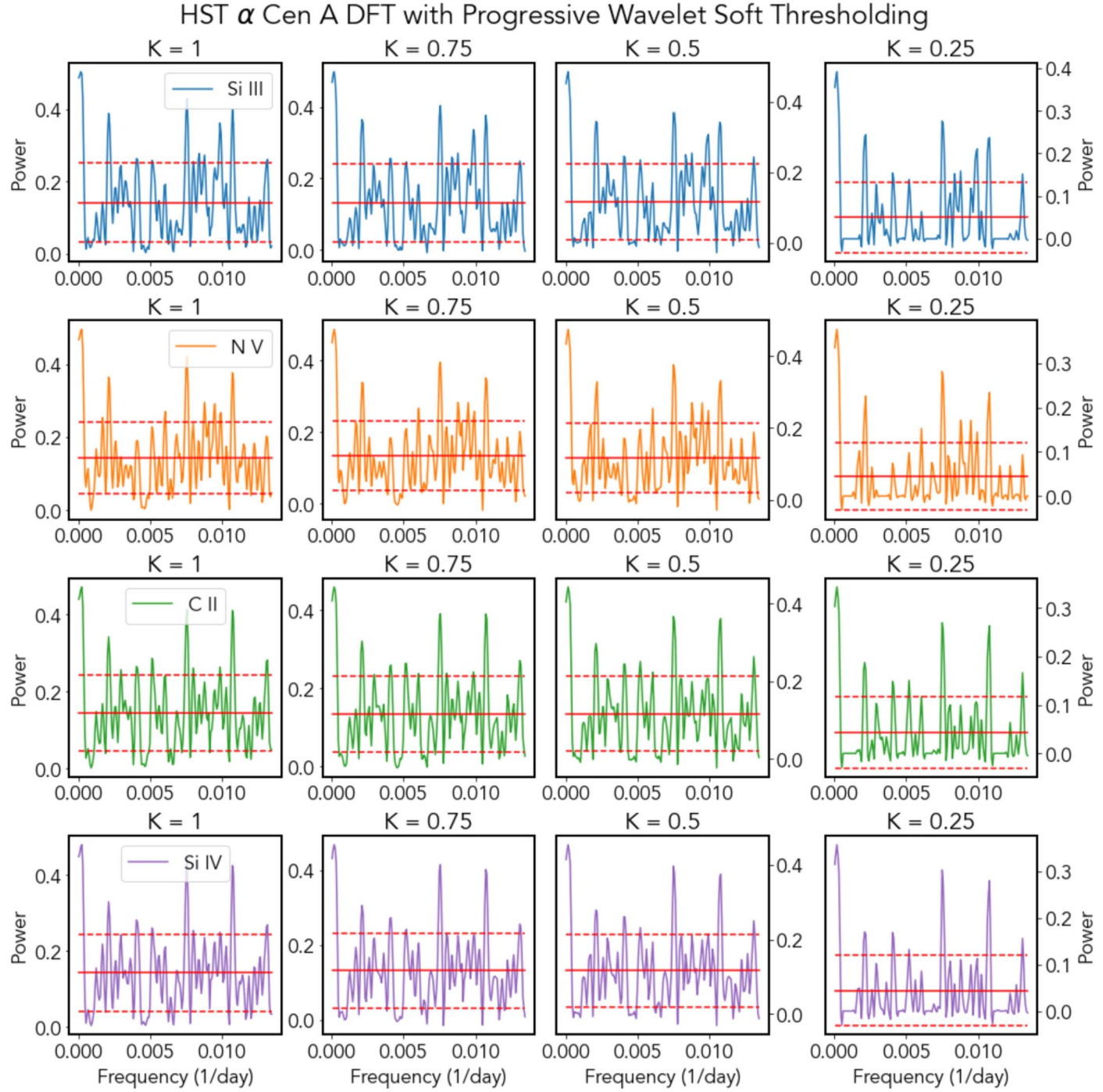


**Figure 5.** Discrete Fourier transform of HST time series data of  $\alpha$  Centauri A for each ion is displayed in the left-most column. Each subsequent column represents progressively greater wavelet soft thresholding.  $K$  (Keep coefficient) is % of wavelet coefficients above threshold. The columns are, from left to right, 100%, 75%, 50%, 25%, respectively. The solid red line indicates the mean power across the entire frequency-domain, while the dotted red line indicates  $1\sigma$  (Standard deviation) away from the mean.

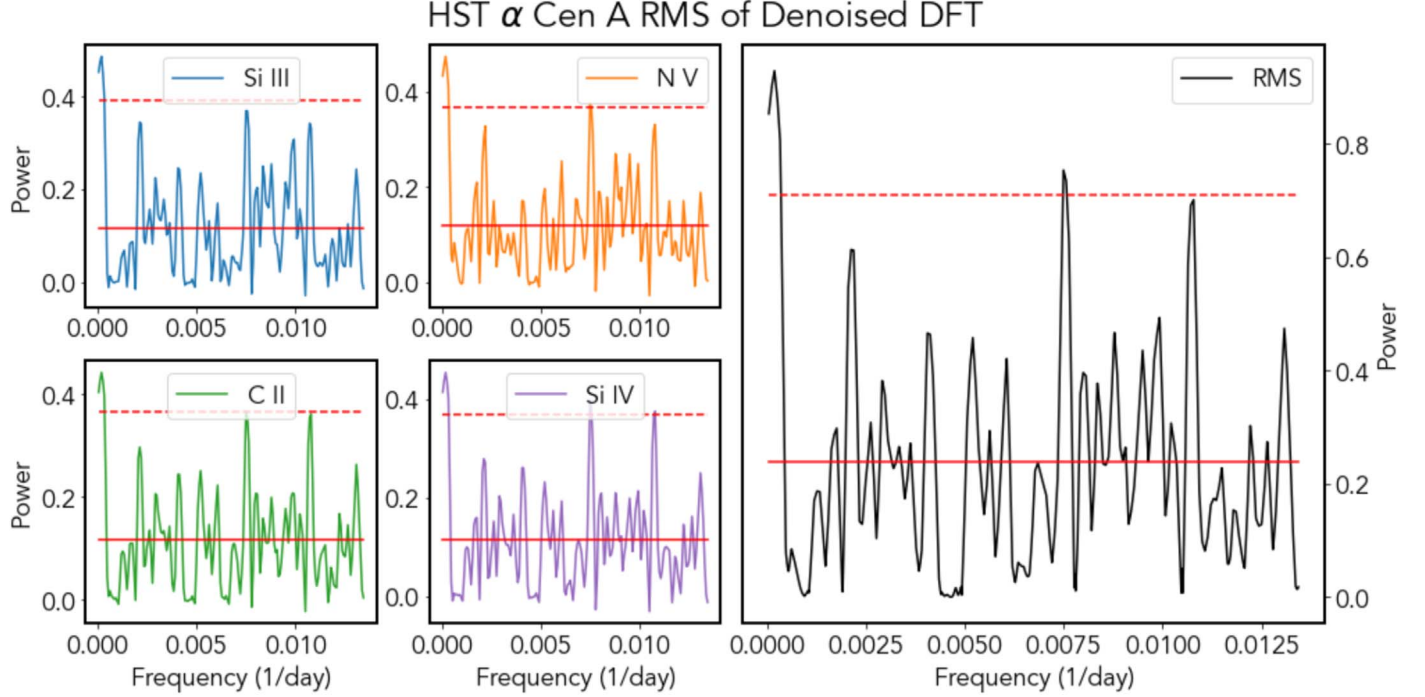


**Figure 6.** Discrete Fourier transform of HST  $\alpha$  Centauri A, with a wavelet soft threshold of  $K = 0.5$  (left 4). Rms combination of all ions (right). The solid red line indicates the mean power across the entire frequency-domain, while the dotted red line indicates  $2.58\sigma$  (Standard deviation) away from the mean (99% confidence interval).

With the `scipy` package (Virtanen et al. 2020), we linearly interpolate the ion frequency decompositions of a selected column of Figure 5 to a common frequency map. Then, we calculate the rms of the four ions’ frequency decompositions to get a comprehensive description of the UV emission periodicity of a particular star (Figure 6).

We determine significant periods by searching for peaks  $>2.58\sigma$  above the mean (corresponding to a significance level of 99%). It should be noted that calculations regarding the presence of significant peaks can be distorted by sample size and distribution of measurements. This can lead to artificial period measurements at the extremes, and as a result, we disregard peak periods that are larger than the total length of observation for a specific star.

We summarize here of the most significant periods for each star (Figures 6, 10, 11, 12, 13): HST  $\alpha$  Centauri A: 133.5 days (Significance  $\approx 2.8\sigma$ ), HST  $\alpha$  Centauri B: 209.2 days (Significance  $\approx 3\sigma$ ), IUE  $\alpha$  Centauri B: 210.1 days (Significance  $\approx 3.7\sigma$ ), IUE  $\epsilon$  Eri: 156.3 days (Significance  $\approx 3.5\sigma$ ), and IUE  $\xi$  Boo: 79.0 days (Significance  $\approx 6\sigma$ ). The concurrence between the measurements obtained from both HST and IUE for  $\alpha$  Centauri B, exhibiting a high level of statistical significance, suggests the existence of a cycle in the stellar UV activity of  $\alpha$  Centauri B with a period of approximately 210 days.

#### 4. Results: Modest Long Term FUV Variability on Most Cool Stars

Figure 4(c) shows that an increase in the effective temperature of a star, which is an indication of its mass, is associated with decreased relative variability in the chromosphere of the star as traced by the observed UV lines. Our sample of stars in this study primarily comprises of cool stars with spectral types ranging from M to F, corresponding to effective temperatures of roughly 3000–7000 K and stellar masses of approximately  $0.1\text{--}2.0 M_{\odot}$ . As stars age, most spectral types exhibit a significant decline in the magnitude of fractional power of UV flux compared to bolometric flux. This decline in fractional UV flux begins rapidly in the more massive cool stars (F, G, and K type), but it remains constant for M type stars up to ages of  $240 \pm 30$  Myr (Loyd et al. 2021), indicating a slower UV evolution for low-mass stars (and even slower for the lowest mass stars, Pineda et al. 2021). Consequently, many M type stars have higher fractional UV flux than their more massive counterparts, resulting in higher UV energy per unit power than F, G, and K stars. UV flux is strongly linked to the magnetic activity within a star, as UV energy is emitted from the upper atmosphere of a star. Therefore, greater fractional UV flux is associated with more magnetically active upper stellar atmospheres

(Wood et al. 1997), leading to higher relative variability. This negative correlation between effective temperature and relative variability supports our findings.

In Figure 4(e), a weak (with a significance of approximately  $2\sigma$ ) positive correlation between the rotational period ( $P_{\text{rot}}$ ) and relative variability ( $\sigma_{\text{rel}}$ ) is demonstrated, which contradicts the expected relationship between rotation and UV activity. Previous studies have shown that cool stars have more intrinsic variability (possibly driven by unresolved stellar flares) and that the rotational period and UV activity obey a power law decline (France et al. 2018). These studies indicate that stars with longer rotational periods have lower levels of UV activity compared to those with shorter rotational periods (e.g., Medina et al. 2020). Further investigation of the data revealed that the positive correlation in our model is driven by an outlier star with high relative variability at a period greater than 80 days (Proxima Centauri). Proxima Centauri has been noted by several studies as anomalously active for its long rotation period (e.g., Davenport 2016). We also found a weaker positive correlation (with a significance of approximately  $1.4\sigma$ ) between the relative variability and the strength of the chromospheric Ca II emission lines in Figure 4(g), which agrees with expected correlations but is not statistically significant. The lack of a strong correlation between stellar activity indicators ( $P_{\text{rot}}$  and  $\log R'_{\text{HK}}$ ) and relative variability may be due to the small number of objects with multi-epoch observing campaigns, as there are few objects with low activity ( $P_{\text{rot}} > 30$  days or  $\log R'_{\text{HK}} < 5.0$ ) in the sample used in this study.

Despite the aforementioned limitations, the analysis presented here indicates that relative variabilities decrease with increasing stellar effective temperature, from 30% to 70% variability for M type stars to  $<30\%$  variability for F, G, and K type stars. We compare our relative variability for late-K and M type stars (those with  $T_{\text{eff}} < 4200$  K) with the temporal variability analysis of Miles & Shkolnik (2017), finding good agreement with their analysis of GALEX FUV fluxes (theirs being  $<50\%$ ). Slight disagreement can be attributed to calculations regarding a single outlier, Proxima Centauri, driving high variability of 76.5% (Table 3). Compared to the significant and periodic stellar X-ray emission seen on timescales of years in the Sun and nearby solar-type stars (Ayres 2014, 2020), our results indicate a lack of significant FUV variability among cool stars on a large scale. The large amplitude peaks in relative maximum values are only observed in very active stars and close binaries, and there are no corresponding minimum observed. This result is supported by individual FUV studies of solar-type stars with IUE and HST (Ayres 1991, 2015). As a result, for single stars and non-interacting binaries, the FUV fluxes observed in a quiescent spectrum should be representative of the average quiescent flux of the star at timescales of years.

In efforts to further understand the significance of the various periodic signatures discovered within the flux output of  $\alpha$

Centauri A,  $\alpha$  Centauri B,  $\epsilon$  Eri, and  $\xi$  Boo, we examine potential sources with relations to known properties of these stars.  $\xi$  Boo, with a period of 79 days, defined by its significance of  $\approx 6\sigma$ , does not match any known periodic sources. The  $\xi$  Boo system is composed of two stars, A and B, which have a orbit of 151 yr, with individual rotations of 6.2 days 11.5 days, respectively. As a result, the 79 days frequency does not naturally follow from these properties. Similarly,  $\alpha$  Centauri B, with a period of 210 days, with a corresponding significance of  $\approx 3\sigma$ , has an orbit with  $\alpha$  Centauri A of 79.7 yr, with a rotation period of 36.7 days. We note that we did not recover the multi-year X-ray cycles of  $\alpha$  Centauri A or B (Ayres 2014, 2020) in our FUV analysis (consistent with the findings of Ayres 2015). Additional analysis of archival and new Ca II  $R'_{\text{HK}}$  measurements may be a promising direction for understanding the origin of these signals.

#### 4.1. Implications for Stellar Extreme Ultraviolet Variability

France et al. (2018) developed an empirical relationship between the fractional luminosity in N V and Si IV ions analyzed here (the fractional luminosity is defined as the ratio of the ion luminosity to the bolometric luminosity,  $L_{\text{ion}}/L_{\text{bol}}$ ) and the fractional 90–360 Å extreme ultraviolet (EUV) luminosity derived from ISM-corrected spectra from the Extreme-Ultraviolet Explorer. The stars used in that relation spanned mid-M to F-type stars with a range of stellar activity, showing no apparent dependence on stellar mass or age. Therefore, the overall low-level of FUV emission line variability on the timescale of years found in this study suggests a similarly modest level of EUV variability in cool stars.

This study suggests that outside of close binary stars and large flare events, the EUV output of cool stars varies less than a factor of two for all cool stars and less than 50% for FGK stars on stellar activity timescales. This finding is consistent with solar measurements in the AIA 171 Å band acquired from 2010 to 2014 and TIMED observations of the He II 304 Å solar emission line variability seen in TIMED observations acquired from 2008 to 2019.<sup>3</sup> The inferred lack of significant EUV variability on timescales of years is contrasted with significant EUV variability on timescales of minutes from, e.g., stellar flares (Audard et al. 2000; France et al. 2020), and the change in the EUV output of cool stars on stellar evolutionary timescales (Ribas et al. 2016; Johnstone et al. 2021; Pineda et al. 2021).

<sup>3</sup> Solar data was retrieved from the LASP LISIRD database—<https://lasp.colorado.edu/lisird/>.

## 5. Summary

Exoplanetary atmospheres are affected by UV radiation inputs from their host stars at a wide variety of timescales, which can influence the photochemical equilibrium of exoplanetary atmospheric conditions and their susceptibility to atmospheric escape. While studies of X-ray/UV flare properties and long-term stellar evolution of exoplanet host stars have shed light on constraints regarding stellar inputs to exoplanetary systems, the UV temporal variability of cool stars on the timescale of stellar cycles are not as well explored. This work presented a comprehensive investigation of the temporal UV variability of cool stars. The FUV emission lines that trace the chromosphere and transition region activity were analyzed using data from HST and IUE data archives to evaluate the characteristic variability of cool stars on timescales of years to

decades. We observed that the relative variability of FUV light curves decreases with increasing stellar temperature, and a weak positive trend in the temporal variability with the Ca II  $R'_{HK}$  stellar activity indicator was observed. Additionally, various periodic structures within FUV flux of select data sets were detected. Of these 5 candidates data sets (4 stars), the most significant findings were periodicities within  $\alpha$  Centauri B, visible within the independent observations of HST and IUE. Of the other 3 stars ( $\alpha$  Centauri A,  $\xi$  Boo,  $\epsilon$  Eri), further examination is required in order to identify potential false-periodic sources.

## Appendix A Ion Correlation Panels

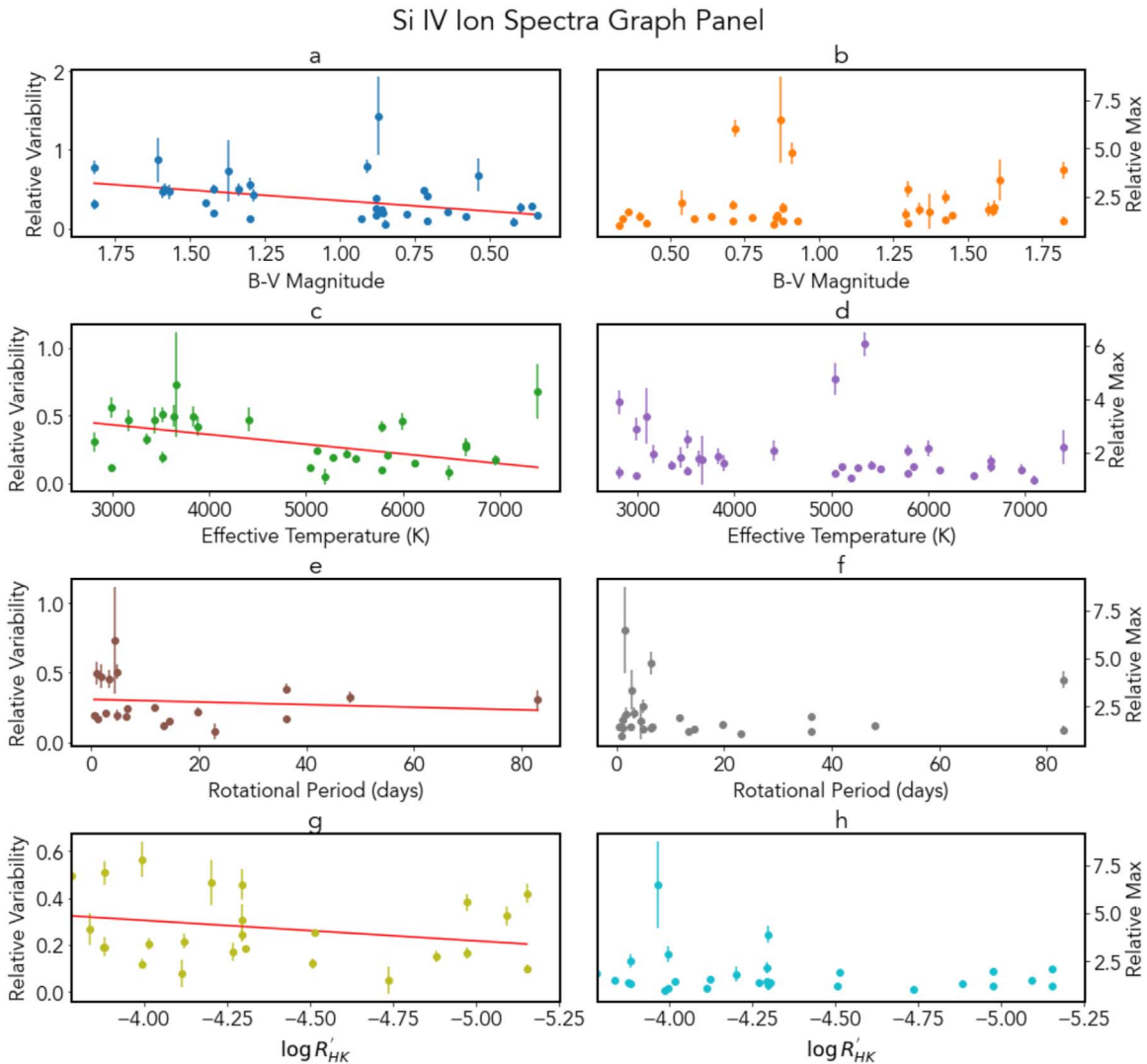


**Figure 7.** Left: correlations of Si IV ion emission variability vs. various stellar parameters with unweighted linear regression depicted with the red lines. Right: relative maximum (maximum divided by the mean) of Si IV ion emission vs. various stellar parameters.

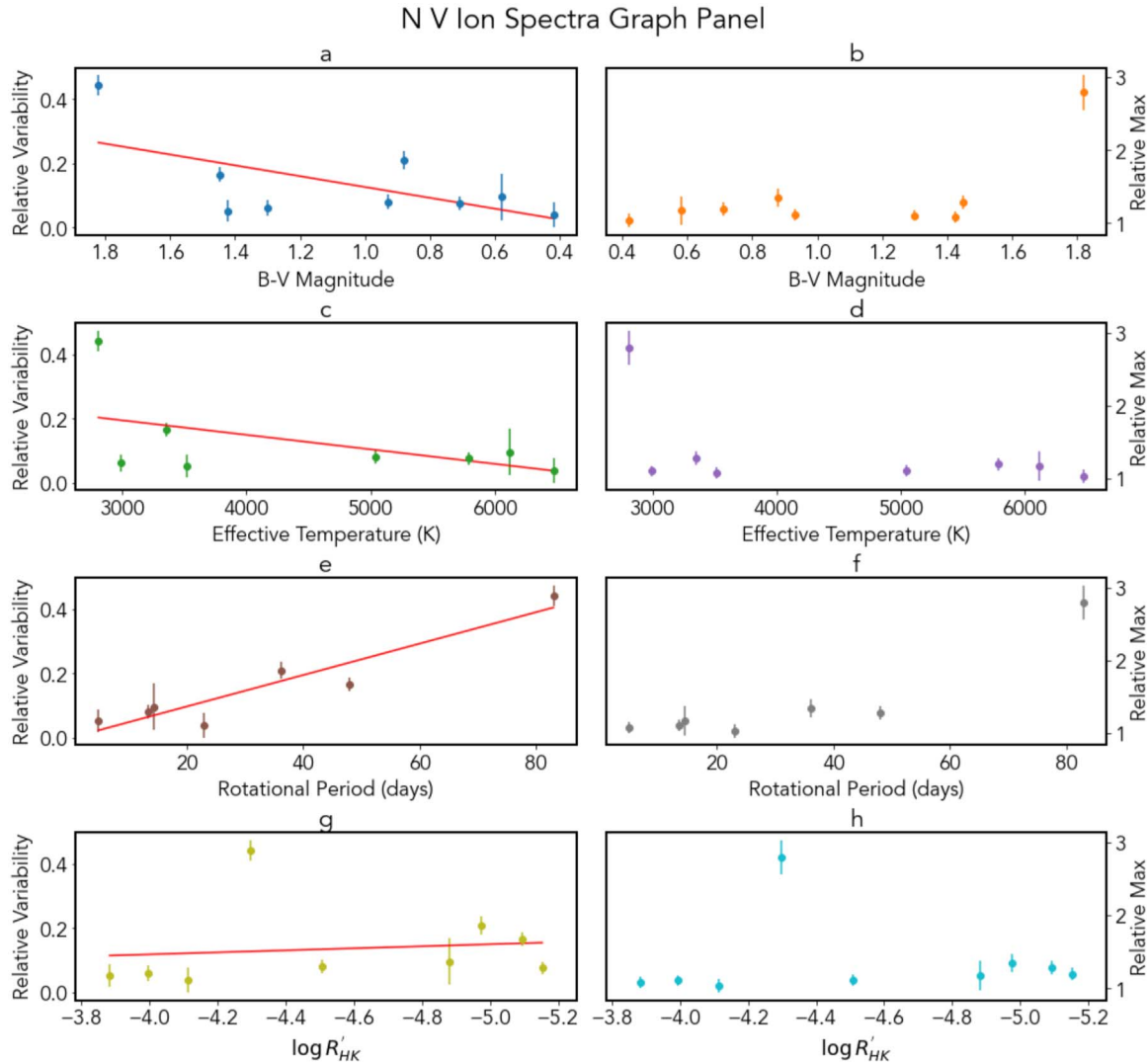


**Figure 8.** Left: correlations of N V ion emission variability vs. various stellar parameters with unweighted linear regression depicted with the red lines. Right: relative maximum (maximum divided by the mean) of N V ion emission vs. various stellar parameters.

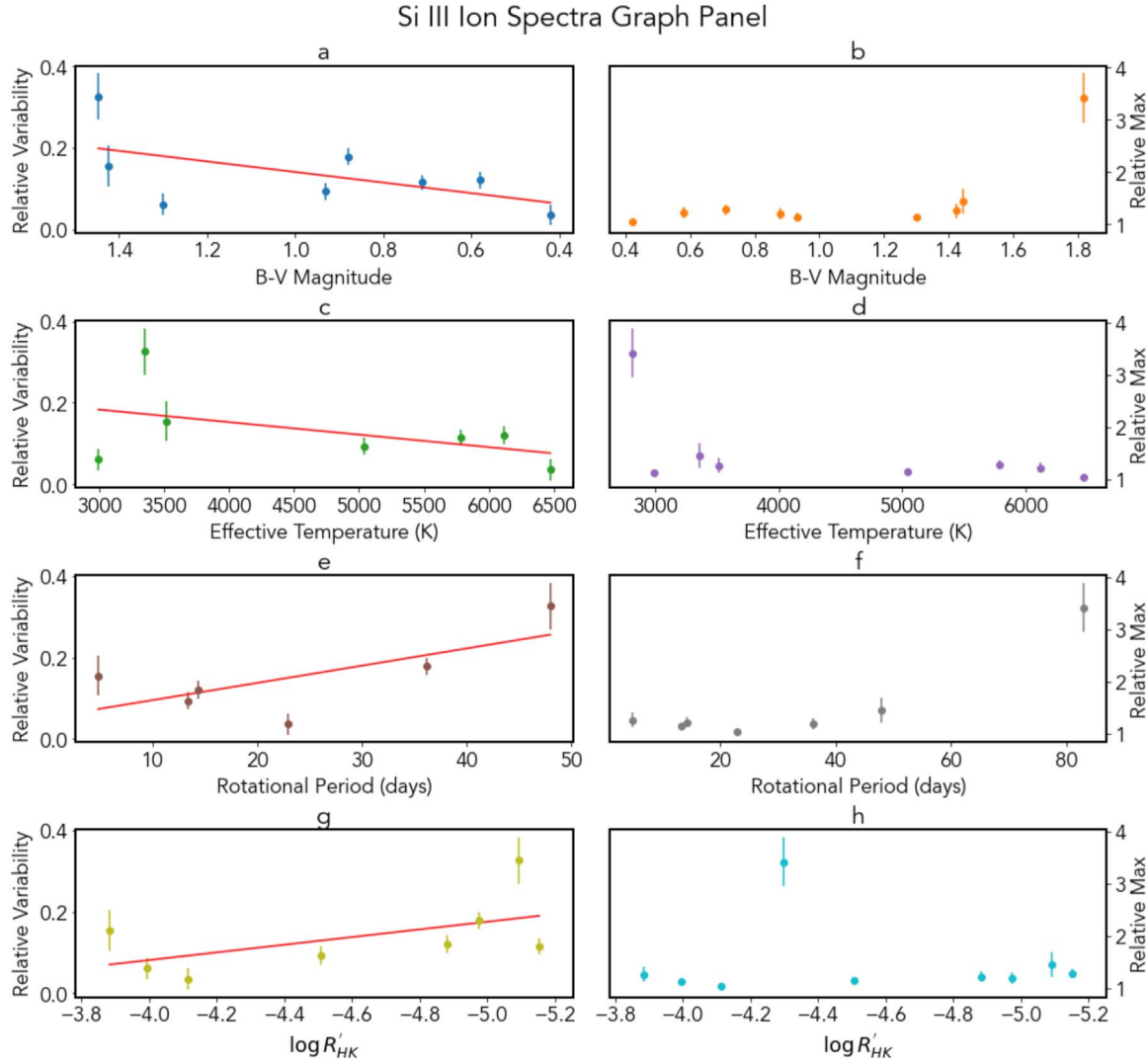


**Figure 9.** Left: correlations of Si III ion emission variability vs. various stellar parameters with unweighted linear regression depicted with the red lines. Right: relative maximum (maximum divided by the mean) of Si III ion emission vs. various stellar parameters.

## Appendix B Rms Denoised DFT Plots

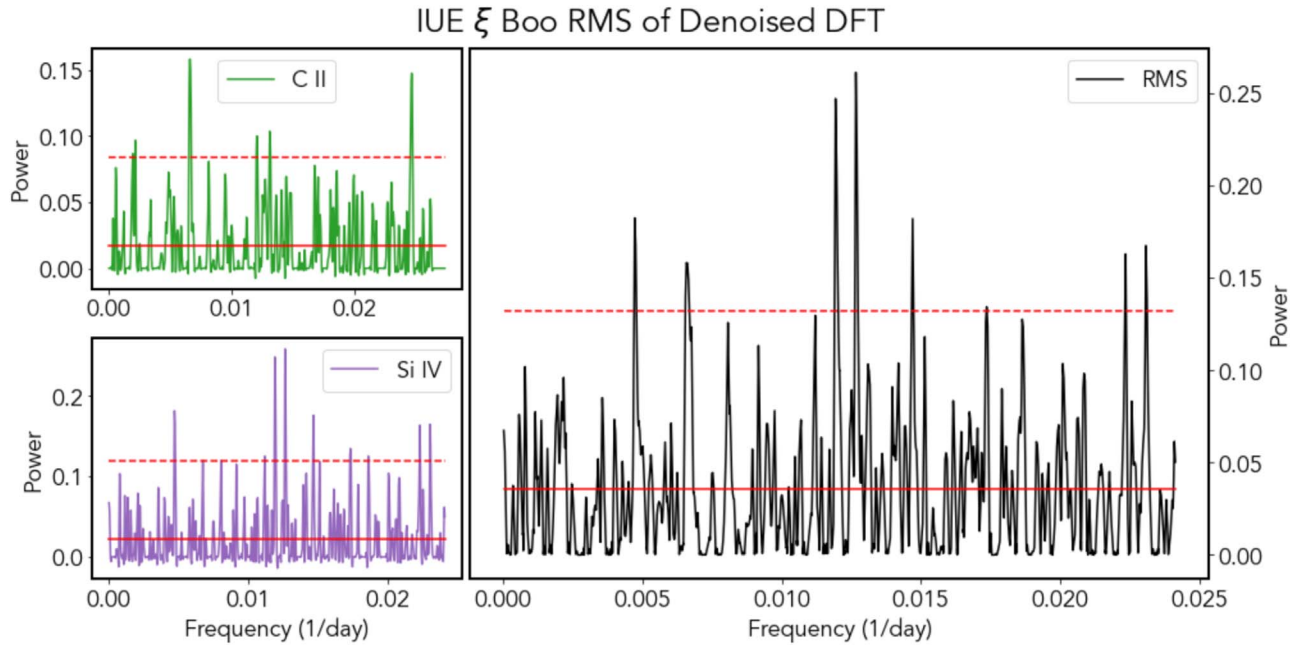


**Figure 10.** Discrete Fourier transform of IUE  $\xi$  Boo, with a wavelet soft threshold of  $K = 0.25$  (left 4). Rms combination of all ions (right). The solid red line indicates the mean power across the entire frequency-domain, while the dotted red line indicates  $2.58\sigma$  (Standard deviation) away from the mean (99% confidence interval).

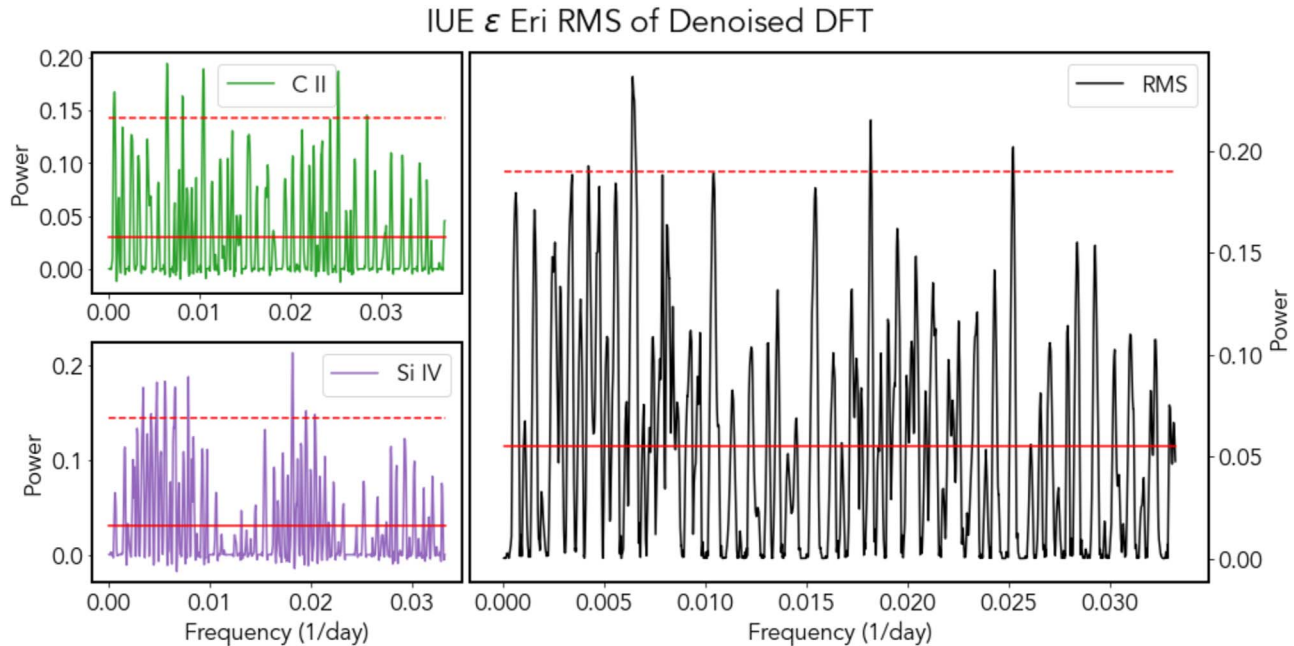


**Figure 11.** Discrete Fourier transform of IUE  $\epsilon$  Eri, with a wavelet soft threshold of  $K = 0.25$  (left 4). Rms combination of all ions (right). The solid red line indicates the mean power across the entire frequency-domain, while the dotted red line indicates  $2.58\sigma$  (Standard deviation) away from the mean (99% confidence interval).

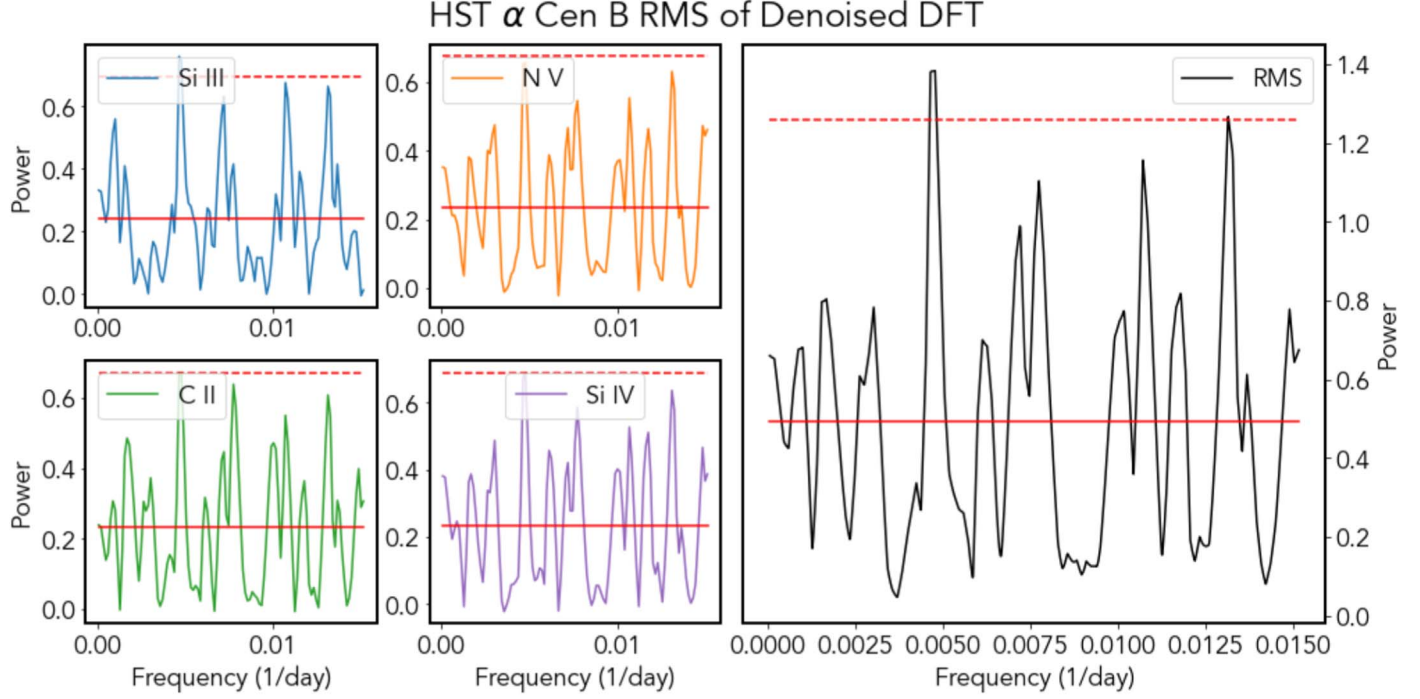


**Figure 12.** Discrete Fourier transform of HST  $\alpha$  Centauri B, with a wavelet soft threshold of  $K = 0.75$  (left 4). Rms combination of all ions (right). The solid red line indicates the mean power across the entire frequency-domain, while the dotted red line indicates  $2.58\sigma$  (Standard deviation) away from the mean (99% confidence interval).

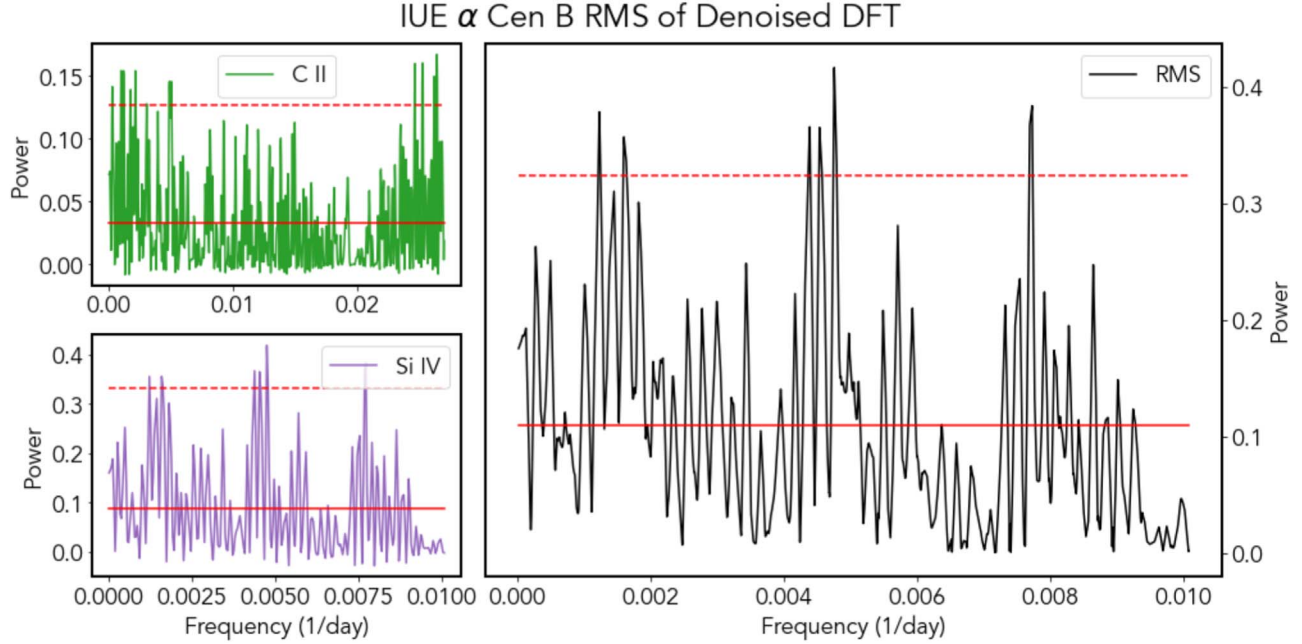


**Figure 13.** Discrete Fourier transform of HST  $\alpha$  Centauri B, with a wavelet soft threshold of  $K = 0.5$  (left 4). Rms combination of all ions (right). The solid red line indicates the mean power across the entire frequency-domain, while the dotted red line indicates  $2.58\sigma$  (Standard deviation) away from the mean (99% confidence interval).

## ORCID iDs

Leo Kamgar <https://orcid.org/0009-0001-6575-9603>  
 Kevin France <https://orcid.org/0000-0002-1002-3674>  
 Allison Youngblood <https://orcid.org/0000-0002-1176-3391>

## References

- Airapetian, V. S., Barnes, R., Cohen, O., et al. 2020, *IJAsB*, **19**, 136  
 Astropy Collaboration, Price-Whelan, A. M., Lim, P. L., et al. 2022, *ApJ*, **935**, 167  
 Audard, M., Güdel, M., Drake, J. J., & Kashyap, V. L. 2000, *ApJ*, **541**, 396  
 Ayres, T. R. 1991, *ApJ*, **375**, 704  
 Ayres, T. R. 2014, *AJ*, **147**, 59  
 Ayres, T. R. 2015, *AJ*, **149**, 58  
 Ayres, T. R. 2020, *ApJS*, **250**, 16  
 Boro Saikia, S., Marvin, C. J., Jeffers, S. V., et al. 2018, *A&A*, **616**, A108  
 Chen, H., Zhan, Z., Youngblood, A., et al. 2021, *NatAs*, **5**, 298  
 Davenport, J. R. A. 2016, *ApJ*, **829**, 23  
 France, K., Arulanantham, N., Fossati, L., et al. 2018, *ApJS*, **239**, 16  
 France, K., Duvvuri, G., Egan, H., et al. 2020, *AJ*, **160**, 237  
 France, K., Parke Loyd, R. O., Youngblood, A., et al. 2016, *ApJ*, **820**, 89  
 Harman, C. E., Schwieterman, E. W., Schottelkotte, J. C., & Kasting, J. F. 2015, *ApJ*, **812**, 137  
 Harris, C. R., Millman, K. J., van der Walt, S. J., et al. 2020, *Natur*, **585**, 357  
 Jackman, J. A. G., Shkolnik, E. L., Million, C., et al. 2023, *MNRAS*, **519**, 3564  
 Jakosky, B., Brain, D., Chaffin, M., et al. 2018, *Icar*, **315**, 146  
 Johnstone, C. P., Bartel, M., & Güdel, M. 2021, *A&A*, **649**, A96  
 Lammer, H., Selsis, F., Ribas, I., et al. 2003, *ApJL*, **598**, L121  
 Lee, G. R., Gommers, R., Waselewski, F., Wohlfahrt, K., & O'Leary, A. 2019, *JOSS*, **4**, 1237  
 Loyd, R. O. P., France, K., Youngblood, A., et al. 2018a, *ApJ*, **867**, 71  
 Loyd, R. O. P., Schneider, P. C., Jackman, J. A. G., et al. 2023, *AJ*, **165**, 146  
 Loyd, R. O. P., Shkolnik, E. L., Schneider, A. C., et al. 2018b, *ApJ*, **867**, 70  
 Loyd, R. O. P., Shkolnik, E. L., Schneider, A. C., et al. 2021, *ApJ*, **907**, 91  
 MacGregor, M. A., Weinberger, A. J., Loyd, R. O. P., et al. 2021, *ApJL*, **911**, L25  
 Medina, A. A., Winters, J. G., Irwin, J. M., & Charbonneau, D. 2020, *ApJ*, **905**, 107  
 Miguel, Y., & Kaltenegger, L. 2014, *ApJ*, **780**, 166  
 Miles, B. E., & Shkolnik, E. L. 2017, *AJ*, **154**, 67  
 Osten, R. A., & Brown, A. 1999, *ApJ*, **515**, 746  
 Pineda, J. S., Youngblood, A., & France, K. 2021, *ApJ*, **911**, 111  
 Ribas, I., Bolmont, E., Selsis, F., et al. 2016, *A&A*, **596**, A111  
 Teal, D. J., Kempton, E. M. R., Bastelberger, S., Youngblood, A., & Arney, G. 2022, *ApJ*, **927**, 90  
 Tian, F., Kasting, J. F., Liu, H.-L., & Roble, R. G. 2008, *JGRE*, **113**, 5008  
 Tsai, S.-M., Lee, E. K. H., Powell, D., et al. 2023, *Natur*, **617**, 483  
 Virtanen, P., Gommers, R., Oliphant, T. E., et al. 2020, *NatMe*, **17**, 261  
 Wood, B. E., Linsky, J. L., & Ayres, T. R. 1997, *ApJ*, **478**, 745